

Enriched photosensitizer for deep-seated-tumor photodynamic therapy

HONGRUI SHAN,^{1,†} XUEQIAN WANG,^{2,†} QIHENG WEI,^{1,†} HAILANG DAI,^{1,4}  AND XIANFENG CHEN^{1,3,5}

¹State Key Laboratory on Fiber Optic Local Area Communication Networks and Advanced Optical Communication Systems, Department of Physics and Astronomy, Shanghai Jiao Tong University, Shanghai 200240, China

²State Key Laboratory of Metal Matrix Composites, Shanghai Key Laboratory for Molecular Engineering of Chiral Drugs, School of Materials Science and Engineering, Shanghai Jiao Tong University, Shanghai 200240, China

³Collaborative Innovation Center of Light Manipulations and Applications, Shandong Normal University, Jinan 250358, China

⁴e-mail: hailangdai@sjtu.edu.cn

⁵e-mail: xfchen@sjtu.edu.cn

[†]These authors contributed equally to this work.

Received 7 December 2023; revised 14 March 2024; accepted 14 March 2024; posted 15 March 2024 (Doc. ID 515233); published 1 May 2024

Photodynamic therapy (PDT) is an innovative approach that utilizes photochemical reactions for non-invasive disease treatment. Conventional PDT is limited by the low penetration depth of visible light required for activation. Herein, we employed upconversion nanoparticles (UCNPs) to extend the activation wavelength of photosensitizers into the infrared range, enabling a treatment depth of over 10 mm. Furthermore, we also used the abundant amino groups of branched polyethyleneimine (PEI) with spatial structure to enhance the loading capacity of protoporphyrin (PPIX), and we ultimately improved skin tumor clearance rates. Moreover, we achieved tumor-specific treatment by utilizing folic acid (FA) targeting and active enrichment of PPIX. According to cellular experimental results, we demonstrated the remarkable reactive oxygen species generation capability of the material and ultra-low dark toxicity. Additionally, we investigated the apoptosis mechanism and demonstrated that the synthesized nanoparticle stimulates the up-regulation of apoptosis-associated proteins Bax/Bcl-2 and Cyto c. During *in vivo* experiments involving intravenous injection in mouse tails, we investigated the anticancer efficacy of the nanoparticle, confirming its excellent PDT effects. This research provides a promising avenue for future non-invasive treatment of deep-seated tumors, offering a method for the treatment and management of specific cancers. © 2024 Chinese Laser Press

<https://doi.org/10.1364/PRJ.515233>

1. INTRODUCTION

Photodynamic therapy (PDT) is an emerging therapeutic modality that harnesses the interaction between photosensitizers, light, and molecular oxygen to selectively destroy cancer cells [1,2]. However, the current application of PDT is primarily focused on treating superficial or shallow tissue tumors. This restriction stems from the fact that the photosensitizers of traditional PDT predominantly respond to visible light, which has poor penetration into deep tissues due to the absorption of most biomolecules, thereby limiting its efficacy in treating deep-seated tumors [3]. To achieve greater light penetration depth, near-infrared (NIR) light has emerged as an ideal option due to its lower absorption by most biological tissues within the NIR window (700–1700 nm) [4–7]. NIR light possesses enhanced tissue-penetrating capabilities, allowing for more efficient penetration of deep-seated tumors and activation of photosensitizers, thus improving the effectiveness of PDT [6]. The combination of NIR light with suited photosensitizers

enables deeper eradication of cancer cells and reduces damage to surrounding normal tissues [3,8,9].

To overcome the limitations of light penetration in PDT, upconversion nanoparticles (UCNPs) have been extensively investigated as promising candidates [10–16]. Researchers have synthesized UCNPs with various properties by controlling their composition, structure, and surface modifications to further optimize their performance [12,17–21]. For instance, doping with rare-earth ions such as erbium, gallium, and yttrium enables different upconversion spectra ranging from near-infrared to visible light [19,22,23]. Additionally, factors such as the size, shape, and coating materials of the nanocrystals can influence the performance of UCNPs, including upconversion efficiency, photostability, and biocompatibility [18,22,24–26]. Besides, UCNPs have demonstrated broad application prospects not only as light sources in PDT but also in areas such as biological imaging [11,27–31], drug release [11,32], and photothermal therapy [11,27,33]. In PDT treatment, UCNPs convert

near-infrared (NIR) light into higher-energy visible or ultraviolet light, enabling deeper tissue penetration and activation of photosensitizers at their optimal wavelengths for therapeutic effects [2,7,30,34]. Additionally, UCNPs synthesized with precision can attain energy transfer efficiencies near 60%, ensuring effective energy conversion even in deep tissues [35]. This makes UCNPs an ideal platform for enhancing the efficacy of PDT. Furthermore, the integration of UCNPs with photosensitizers is crucial as it directly influences the efficiency of reactive oxygen species (ROS) generation. Among various photosensitizers, protoporphyrin (PPIX) has garnered significant attention due to its favorable photophysical properties, biocompatibility, and clinical applicability [36–41]. However, existing studies faced challenges such as limited and unstable photosensitizer loading of UCNPs, making it difficult to achieve sufficient ROS concentrations for effective tumor destruction, despite achieving enhanced light penetration depth [10]. Meanwhile, UCNPs cannot be actively enriched in the tumor site due to the lack of specific recognition ability. The primary challenge in cancer therapy is the disruption of the balance between cancerous and normal tissues during treatment. Due to physiological and microenvironmental differences between tumor and normal tissues, an increasing number of materials are being developed for targeted tumor therapy. Folic acid is widely used by researchers due to its affordability, accessibility, non-toxicity, non-immunogenicity, and high affinity to folate receptors [42]. Based on this, we are seeking a more efficient method in PDT, by which UCNPs with abundant photosensitizers can specifically gather into tumor tissues, to generate a lot of ROS and then improve tumor clearance rates in deep-seated tumors.

In this study, a novel composite material, PPIX-PEI-UCNP@FA NPs, was synthesized [Fig. 1(a)], comprising PPIX molecules, UCNPs doped with ytterbium (Yb) and erbium (Er), PEI, and FA. Current modifications of UCNPs with PEI typically involve a surface coating layer of PEI, which does not exploit the potential spatial structure provided by PEI to achieve higher drug loading and enhanced light absorption efficiency [43]. However, clinically, the high cytotoxicity of PEI is the main barrier to the safe use of PEI-coated nanomaterials. PEI has significant toxicity due to high polycationic charge density generated by a large number of amino groups. It can cause

severe membrane damage inducing necrotic or apoptotic processes. In our work, the highly branched PEI rich in amino groups was used to link surface bifunctionalized UCNPs, forming a 3D structure with a high specific surface area, centered around PPIX-loaded UCNP nodes. This architecture achieved a porphyrin loading rate of up to 0.69% (mass fraction). PPIX was loaded onto the UCNPs and crosslinked with the 3D network formed by PEI as well, resulting in a higher loading capacity compared to previous strategies. Moreover, being crosslinked with PPIX blocked the amino groups in PEI, thus reducing its toxicity by diminishing the polycationic charge (because of less cationic ligands interacting with cells) through triple PPIX conjunction, while effectively reducing PEI toxicity by utilizing amine groups. The UCNPs extended the excitation wavelength to 980 nm, allowing therapeutic penetration beyond 10 mm. The branched PEI enhanced the loading efficiency of PPIX, leading to effective singlet oxygen generation and high tumor cell kill rates. The functionalization with folic acid (FA) enabled targeted drug delivery to cancer cells. The PPIX-PEI-UCNP@FA nanoparticles demonstrated properties of near-infrared excitation, deep tissue penetration, high ROS production, and tumor-specific targeting. Compared to PPIX loaded PLGA-PEG NPs [44], our material achieves a 3-fold increase in drug loading and lower toxicity, and nearly triples ROS production in deep tissue. Benefiting from the high loading capacity offered by the spatial structure of PEI, our approach has doubled the targeting efficiency compared to systems without PEI. *In vivo*, after intravenous injection, the material binds to FA receptors on tumor cell membranes, internalizes, and, upon 980 nm laser exposure, generates ROS in deeper skin tumors. This study's findings are crucial for advancing PDT, overcoming traditional limitations, and enhancing clinical outcomes in cancer treatment [Fig. 1(b)]. Administered intravenously in mice, the NPs bind to tumor cell membrane FA receptors and internalize, acting within mitochondria. Upon 980 nm laser exposure, they generate excessive ROS in deeper skin tumors, impairing mitochondrial function, decreasing MMP, and reducing ATP production. Activation of apoptosis-associated proteins via the mitochondrial-dependent pathway leads to the destruction of tumor cells. These findings are crucial for developing advanced PDT strategies, overcoming traditional limitations, and enhancing clinical outcomes in cancer treatment.

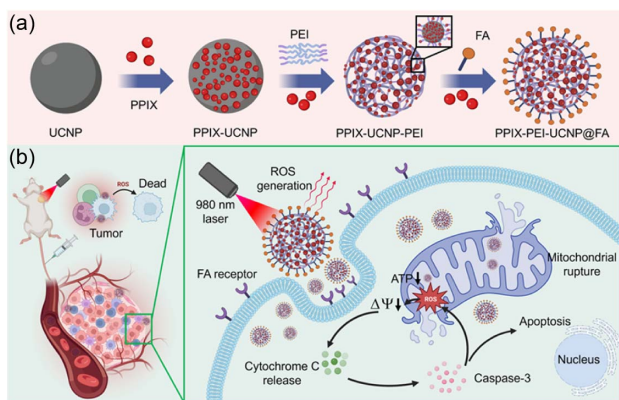


Fig. 1. (a) Scheme of synthesis of PPIX-PEI-UCNP@FA NPs. (b) Mechanism of PPIX-PEI-UCNP@FA NPs as the PDT agent for tumor therapy via the 980 nm laser.

2. RESULTS AND DISCUSSION

Nanoparticle synthesis and analysis. To prepare the materials for the experiments, we initially synthesized upconversion nanoparticles (UCNPs) with a core-shell structure, exhibiting high fluorescence intensity (for detailed procedures, refer to the Section 4). As shown in Fig. 2(a), the transmission electron microscope (TEM) images reveal uniform and well-dispersed spherical UCNPs with an average size of 30 nm. The Fourier-transform infrared spectroscopy (FTIR) analysis of the UCNPs' surface organic ligands [Fig. 2(b), black line] reveals distinct absorption peaks at 2920 cm^{-1} and 2853 cm^{-1} , corresponding to the stretching vibrations of C-H bonds. Additionally, an absorption peak at 1552 cm^{-1} corresponds to the vibrations of C=O and C=C bonds, while the peak at 1455 cm^{-1}

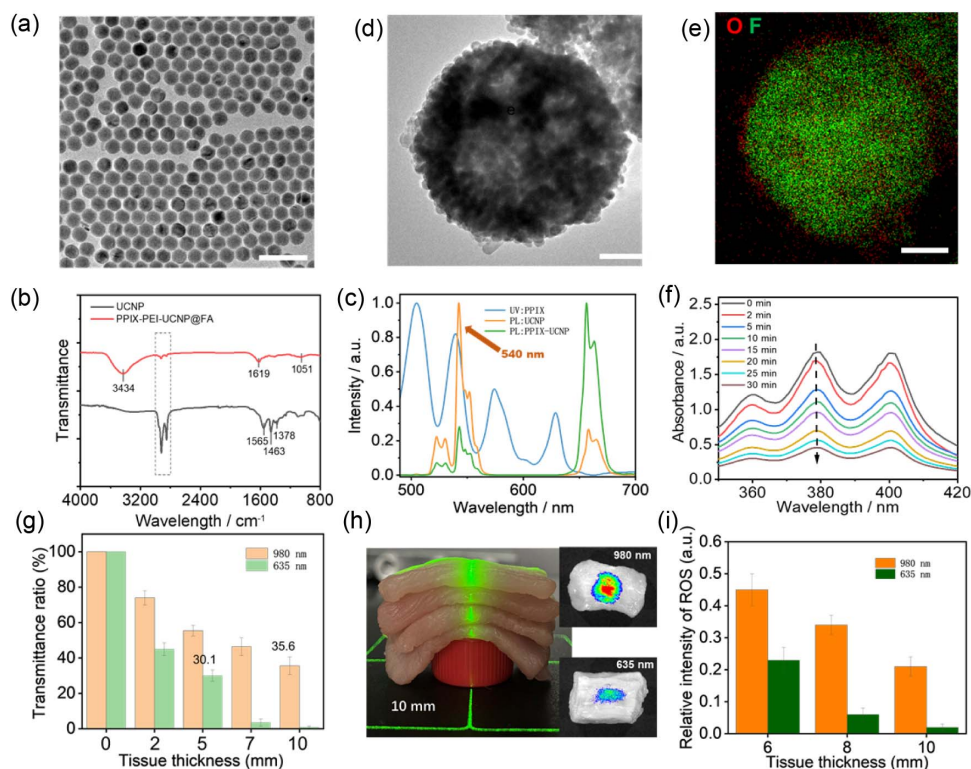


Fig. 2. Synthesis and characterization of PPIX-PEI-UCNP@FA NPs as an agent of PDT. (a) The transmission electron microscopy (TEM) image of UCNPs (scale bar: 100 μm). (b) The Fourier-transform infrared spectroscopy (FTIR) analysis of the UCNPs and of PPIX-PEI-UCNP@FA NPs. (c) UV-visible absorption spectrum of PPIX and photoluminescence spectrum of UCNPs and PPIX-UCNPs with the 980 nm laser. (d) High angle annular dark field (HAADF) image of PPIX-UCNPs from TEM (scale bar: 100 μm). (e) An overlap of scanning TEM (STEM) mapping image of O and F elements. (f) Time-dependent UV-visible absorption spectra of the PPIX-PEI-UCNP@FA NPs and ABDA mixture solution upon 980 nm laser irradiation at 1 W/cm² (scale bar: 100 μm). (g) Penetration depth of 980 nm and 635 nm lasers in different thicknesses of porcine tissue. (h) Spot profiles of 980 nm and 635 nm laser beams after passing through 10 mm porcine tissue. (i) ROS generation after 30 min of 980 nm and 635 nm laser irradiation through different thicknesses of porcine tissue.

corresponds to the bending vibrations of C-H bonds. Based on these observations, it can be inferred that the ligands on the surface of the UCNPs are oleic acids. As a commonly used surfactant, oleic acid effectively prevents nanoparticle aggregation, facilitating their cellular uptake and enhancing the generation of reactive oxygen species (ROS) upon excitation by light. In order to investigate the fluorescence properties of the synthesized UCNPs, we employed a 980 nm near-infrared laser as the excitation light source to measure the upconversion fluorescence spectrum of the UCNPs [Fig. 2(c), orange line]. The results revealed three distinct emission peaks within the range of 500–700 nm. Specifically, there were two green emission peaks located at 525 nm and 545 nm, as well as a weak red emission peak at 660 nm. These emission peaks correspond to the transitions of erbium ions: $^2\text{H}_{11/2} \rightarrow ^4\text{I}_{15/2}$, $^4\text{S}_{3/2} \rightarrow ^4\text{I}_{15/2}$, and $^4\text{F}_{9/2} \rightarrow ^4\text{I}_{15/2}$, respectively.

Subsequently, we employed a one-step self-assembly and chemical synthesis approach to encapsulate the photosensitizer PPIX onto the surface of the core-shell structured upconversion nanomaterial. To enhance the loading capacity of the final product for PPIX, we utilized polyethyleneimine (PEI), rich in abundant amino groups, as the framework of the end product. Through amidation with the carboxyl groups in PPIX, we obtained PPIX-PEI-UCNPs with an average particle size of

approximately 387 nm. The nanomaterials were also analyzed using scanning TEM (STEM) coupled with energy dispersive spectroscopy (EDS) to confirm the composition of nanoparticles. The high-angle annular dark-field (HAADF) STEM image in Fig. 2(d) also shows a clear structure of PPIX-PEI-UCNPs. An overlay of O and F element EDS mapping image is shown in Fig. 2(e), illustrating the uniform distribution of O element from the original PPIX throughout the entire nanoparticle, forming the outer layer that encases the inner core containing F element from the UCNPs. This indicates the successful composite formation of PPIX-UCNPs, facilitated by PEI assistance.

To extend the activation wavelength of PPIX to the near-infrared range (980 nm), fluorescence resonance energy transfer (FRET) between UCNPs and PPIX is required. For FRET to occur, the donor's emission peak must overlap to some extent with the acceptor's absorption peak. As shown in Fig. 2(c) (blue line), PPIX exhibits several gradually decreasing absorption peaks between 500 nm to 650 nm, while the main absorption peak of the UCNPs is around 980 nm, with distinct upconversion emission peaks at approximately 540 nm and weaker emission peaks at 525 nm and 660 nm. It is evident that the emission peak of UCNPs at around 540 nm significantly overlaps with the absorption peak of PPIX, fulfilling the basic

condition for fluorescence resonance energy transfer. Additionally, the core-shell structure of the UCNP allows for a certain distance between the donor and acceptor, which further supports the occurrence of FRET. By measuring the fluorescence spectrum of PPIX-UCNPs, a significant decrease in the fluorescence intensity at 540 nm compared to UCNP's fluorescence spectrum confirms that PPIX absorbs high-energy photons emitted by UCNP [Fig. 2(c), green line]. Besides, the emission peak of porphyrin appeared at 660 nm. Thus, we successfully utilized UCNP to extend the excitation wavelength of the photosensitizer PPIX to the near-infrared range through efficient FRET.

In order to achieve specific targeting of tumor cells, increase the drug concentration inside the cells, and reduce the damage to normal cells, we introduced folate (FA) to PPIX-PEI-UCNP. Studies have confirmed that folate receptors (FRs) are widely expressed on the surface of various tumor cells, while only a small amount is expressed in normal cells. Additionally, folate receptors have high affinity for folate or folate derivatives. Thus, we successfully obtained FA-modified nanomaterials, PPIX-PEI-UCNP@FA NPs, with FR as the target. Based on the infrared spectrum of the composite material [Fig. 2(b), red line], notable changes are observed in the UCNP upon coupling with PPIX and FA. The disappearance of the N-H deformation vibration absorption peak of amino group at 1565 cm^{-1} and the appearance of a new N-H bending vibration strong absorption peak at 1619 cm^{-1} indicate the formation of amide bonds between the amino groups of the UCNP and the FA, confirming their successful coupling. In the range of $3000\text{--}2800\text{ cm}^{-1}$, characteristic absorption peaks are present in the spectrum of the new composite, which verifies the presence of UCNP. The N-H stretching vibration peak at 3434 cm^{-1} and the porphyrin skeleton vibration peak at around 1000 cm^{-1} confirm the presence of PPIX. The Zetasizer Nano analyzer measurement revealed that the materials carry a negative charge (-3.7 mV), which facilitates their accumulation in tumor sites through the bloodstream for an extended period. Furthermore, these nanomaterials are internalized by tumor cells with high expression of folate receptors through receptor-specific interactions. Under light activation, targeted therapy for tumors is achieved, thanks to the specific binding of FA to the folate receptors on tumor cells. Finally, to validate the photodynamic therapy efficacy of PPIX-PEI-UCNP@FA NPs, we used 9,10-anthracenediyl-bis(methylene)dimalonic acid (ABDA) as an active oxygen probe to test its ability to generate singlet oxygen under near-infrared laser irradiation in an aqueous environment. ABDA can undergo an oxidation-reduction reaction with active oxygen, leading to a reduction in the probe's fluorescence intensity. Figure 2(f) displays the time-dependent UV-visible absorption spectra of the PPIX-PEI-UCNP@FA NPs and ABDA mixture solution upon 980 nm laser irradiation at 1 W/cm^2 . After 30 min of irradiation, the fluorescence intensity decreased to one-sixth of its original value, and ROS was significantly enhanced, demonstrating the material's excellent capability to generate active oxygen. To assess the effectiveness of the composite material in deep tissue, we initially evaluated the tissue penetration depths of both 980 nm and 635 nm lasers. Two lasers were directed

through varying thicknesses of pork tissue, and the transmitted light spots were measured. The results indicated a tissue penetration depth of approximately 10 mm for the 980 nm laser, whereas the 635 nm laser exhibited a penetration depth of less than 5 mm [Fig. 2(g)]. Figure 2(h) displays the spot profiles of the two beams after passing through 10 mm of tissue. For a specific confirmation of the therapeutic effect within deep tissue, separate experiments with the two lasers penetrating different tissue thicknesses were conducted. We measured the amount of generated ROS in the material under 30-min irradiation. As shown in Fig. 2(i), when passing through 10 mm of tissue, the 980 nm laser generates ROS at approximately 10 times the level of the 635 nm laser, which shows an excellent deep tissue killing effect.

***In vitro* evaluation of the anticancer effect induced by PPIX-PEI-UCNP@FA NPs in NIR-triggered PDT.** In order to verify the inhibitory effect of as-synthesized PPIX-PEI-UCNP@FA NPs as photodynamic agents against tumor cells, the cytotoxicity of NPs on mouse breast cancer (4T1) cells was first evaluated by the CCK-8 method *in vitro*. As shown in Fig. 3(a), in the absence of laser irradiation, treatment with different concentrations of PPIX-PEI-UCNP@FA NPs showed no significant cytotoxicity on 4T1 cells, indicating that NPs had low dark toxicity. However, under NIR laser irradiation for 10 min (980 nm, 1.0 W/cm^2), PPIX-PEI-UCNP@FA NPs could induce severe cytotoxicity in 4T1 cells in a concentration-dependent manner. For effectively killing tumor cells, it was calculated that the lowest concentration of PPIX-PEI-UCNP@FA NPs required to reduce the cell survival rate to 50% was $57.84\text{ }\mu\text{g/mL}$; thus, NPs with a concentration of $60\text{ }\mu\text{g/mL}$ were studied in subsequent experiments. Additionally, the cytotoxicity of PPIX-PEI-UCNP@FA NPs was also assessed on normal mouse fibroblast (L929) cells. It could be found that NPs exhibited no obvious cytotoxicity on L929 cells in a dose-independent way, whether laser irradiated or not [Fig. 3(b)]. These findings demonstrated that PPIX-PEI-UCNP@FA NPs exhibited good biological safety, killing tumor cells selectively with a minor effect on the viability of normal cells. Also, normal cells are not significantly affected by the laser irradiation utilized in this study. These results were further confirmed by the use of live and dead labeling both in 4T1 and L929 cells. From the fluorescence images of 4T1 cells, it could be observed that the PPIX-PEI-UCNP@FA NPs combined with laser irradiation caused large amounts of red fluorescence within the cells, and the green fluorescence was noticeably reduced, which was a sign of cell death [Fig. 3(c)]. In contrast, in the other groups, extensive green fluorescence representing live cells was detected, as well as no obvious red fluorescence. Also, large amounts of green fluorescence were observed in L929 cells regardless of whether they were treated with laser irradiation or incubated with NPs. These results from the live/dead observation were in accordance with those from the CCK-8 experiment, where both types of results showed that PPIX-PEI-UCNP@FA NPs could selectively kill cancer cells while having negligible effect on normal cells when triggered by the laser, which is conducive for subsequent *in vivo* tests. Moreover, the killing ability of the NPs on 4T1 cells was quantitatively characterized by flow cytometry. The results of

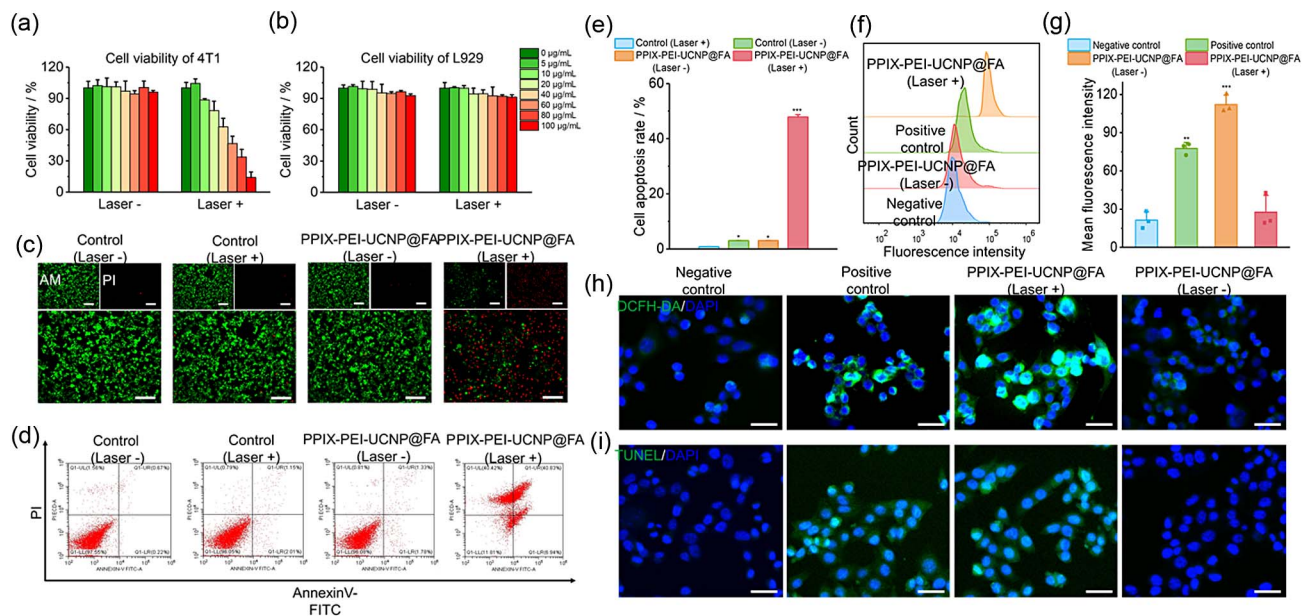


Fig. 3. Cell viability of (a) 4T1 cells and (b) L929 cells after incubation 48 h with different concentrations of PPIX-PEI-UCNP@FA NPs in the presence or absence of laser (980 nm, 1 W cm^{-2}). (c) Live/dead staining images of 4T1 cells with various treatments (scale bar: 250 μm). (d) Flow cytometry results of 4T1 cells co-stained by Annexin V-FITC and PI after different treatments and (e) the corresponding statistics of apoptosis cells. (f) Intracellular reactive oxygen species generation (ROS) evaluated by flow cytometry after different treatments (negative control: without any treatment; positive control: treated with H_2O_2 only). (g) Mean fluorescence intensity statistics of 4T1 cells corresponding to (h). (h) Fluorescence images of intracellular ROS after various treatments using DCFH-DA as the probe (scale bar: 100 μm). (i) TUNEL-stained images of 4T1 cells after different treatments (scale bar: 100 μm).

flow cytometry showed that PPIX-PEI-UCNP@FA NPs could produce high cytotoxicity to 4T1 cells under the induction of laser irradiation, and most cells were located on the right side of the apoptotic profiles, with a maximum of 47.88%. On the contrary, 4T1 cells exposed to the laser alone or treated with PPIX-PEI-UCNP@FA NPs experienced only slight apoptosis, about 3.01% and 3.05%, respectively [Figs. 3(d) and 3(e)].

It has previously been confirmed that PPIX-PEI-UCNP@FA NPs could generate excessive ROS when exposed to the laser, which caused cell damage. Therefore, 2',7'-dichlorofluorescein diacetate (DCFH-DA) as an ROS probe was used to detect the production efficiency of ROS at the cellular level, in which 4T1 cells treated with H_2O_2 were used as the positive control. According to the fluorescence staining images, 4T1 cells treated with H_2O_2 showed substantial amounts of green fluorescence, which indicated that H_2O_2 treatment activated the internal oxidative stress reaction of the cells, prompting them to produce an enormous quantity of ROS [Fig. 3(h)]. Interestingly, a similar increasing phenomenon of strong green intensity was observed after PPIX-PEI-UCNP@FA NPs in NIR-triggered treatment but was negligible in the other groups [Fig. 3(g)]. The quantitative analysis of different treated cells on flow cytometry also showed that PPIX-PEI-UCNP@FA NPs combined with laser irradiation revealed higher levels of intracellular ROS [Fig. 3(f)]. However, in L929 cells, except for the positive control group, there was no excessive production of ROS after different treatments. The apoptotic cells were then accessible via terminal-deoxynucleotidyl transferase-mediated dUTP nick-end-labeling (TUNEL) following different treatments. Representative images of TUNEL

staining for the various treatments are shown in Fig. 3(i). The PPIX-PEI-UCNP@FA NPs group displayed significantly more green fluorescence in the presence of the laser than the negative control group, which was comparable to cells treated with H_2O_2 and indicated a significant quantity of 4T1 cells going through apoptosis. These results suggested that the PPIX-PEI-UCNP@FA NPs could be stimulated by laser irradiation to produce excess ROS and hence induce cell apoptosis.

Mechanism of cell apoptosis induced by PPIX-PEI-UCNP@FA NPs in NIR-triggered PDT. Nanoparticle-based materials could be internalized by cells through phagocytosis or receptor-mediated endocytosis to reach specific sites and finally show therapeutic effects. The intracellular uptake of PPIX-PEI-UCNP@FA NPs by 4T1 cells was observed by confocal laser scanning microscopy (CLSM). Figure 4(a) shows that the red fluorescence of PPIX-PEI-UCNP@FA NPs could be clearly visible in the cells after a certain amount of time of incubation and that the quantity of NPs increased with the extension of time, as reflected by the increased intensity of the red fluorescence. The degree of cellular uptake was also quantitatively examined by flow cytometry [Fig. 4(b)]. The results demonstrated that PPIX-PEI-UCNP@FA NPs could be efficiently internalized by tumor cells since the fluorescence intensity of the NPs steadily arose from 0.5 h to 12 h of incubation with cancer cells. Obviously, this occurrence was related to the conjugation of FA on the surface of NPs, which dramatically assisted cellular uptake through unique interactions between FA and its receptor overexpressed in 4T1 cells.

Mitochondria play an important role in regulating cell function, and redox imbalances in mitochondria could lead to

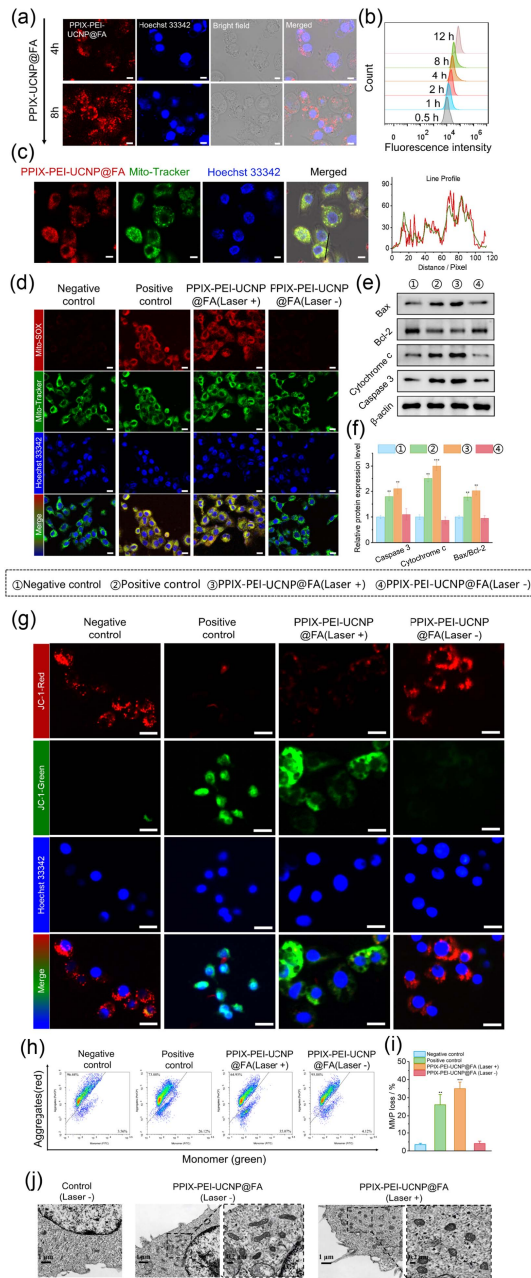


Fig. 4. Cellular uptake of PPIX-PEI-UCNP@FA NPs in 4T1 cells determined by (a) confocal laser scanning microscopy (CLSM, scale bar: 25 μm) and (b) flow cytometry at different times. (c) Colocalization analysis of PPIX-PEI-UCNP@FA NPs and mitochondria using CLSM and the corresponding fluorescent line profile (red line representing PPIX-UCNP NPs and green line representing Mito-Tracker, scale bar: 25 μm). (d) Fluorescent images of mitochondrial ROS production after various treatments (scale bar: 25 μm). (e) Western blot (WB) results of caspase-3, cytochrome c, Bcl-2, and Bax after different treatments. (f) The relative protein expression levels of WB in (e). (g) Fluorescence images of mitochondrial membrane potential in 4T1 cells after different treatments using JC-1 (scale bar: 100 μm). (h) Flow cytometry of mitochondrial membrane potential (MMP) of 4T1 cells after different treatments using JC-1 and (i) the corresponding statistics of MMP loss. (j) BioTEM images of 4T1 cells after incubation with PPIX-PEI-UCNP@FA NPs with or without the laser (980 nm, 1 W cm^{-2}) for 48 h (scale bars: 1 and 0.2 μm).

mitochondrial dysfunction, which may eventually lead to cell death. In order to explore the mechanism of apoptosis induced by PPIX-PEI-UCNP@FA NPs in NIR-triggered PDT, the colocalization of NPs and mitochondria was initially analyzed. With the assistance of CLSM, it could be seen that the green fluorescence of mitochondria overlapped well with the red fluorescence of PPIX-PEI-UCNP@FA NPs after 12 h of incubation, demonstrating that the majority of NPs reached the mitochondria and were co-located with the mitochondria. By analyzing the correlation between mitochondria and PPIX-PEI-UCNP@FA NPs, it could be shown that there was a strong link between mitochondria and PPIX-PEI-UCNP@FA NPs, which suggested that the NPs had a special capacity for targeting mitochondria [Fig. 4(c)]. Then, corresponding fluorescent probes were used to detect ROS production in 4T1 cells after different treatments. The results showed that abundant ROS was induced following incubation of 4T1 cells with PPIX-PEI-UCNP@FA NPs and laser irradiation [Fig. 4(d)]. These excessive ROS may lead to impairment of mitochondrial function and cell death. Compared with the negative control group, the PPIX-PEI-UCNP@FA NPs and laser combination group resulted in a 58.52% decrease in ATP production, which was lower than that of the H_2O_2 -treated group (44.1%), presumably due to the mitochondrial dysfunction induced by the NPs under the laser. Additionally, ROS could cause changes in MMP, which was associated with cell apoptosis. Thus, the change in MMP was determined by a JC-1 probe, which existed in its aggregate state and generated red fluorescence at high MMP, while it appeared in monomer form and emitted green fluorescence under low MMP. It was clearly demonstrated that the majority of JC-1-labeled mitochondria displayed red fluorescence in the absence of lasers or PPIX-PEI-UCNP@FA NPs. In contrast, when the NPs and the laser were incubated with cells, the fluorescence color of the mitochondria dramatically changed from red to green [Fig. 4(g)]. Flow cytometry also revealed a statistically significant reduction (36.2%) in the number of 4T1 cells in the left upper corner corresponding to the JC-1 aggregate form in mitochondria after receiving PPIX-PEI-UCNP@FA NPs and laser treatment, indicating that NPs could damage mitochondrial function under laser excitation [Figs. 4(h) and 4(i)]. Changes in mitochondrial morphology may potentially be indicative of changes in mitochondrial function. In order to better comprehend the alterations in mitochondria, the ultrastructure of different post-treated cells was observed using biological transmission electron microscopy (BioTEM). As shown in Fig. 4(j), the morphology of 4T1 cells was essentially unchanged in the absence of laser or PPIX-PEI-UCNP@FA NPs treatment, while the laser-induced NP group caused severe mitochondrial structural damage, revealing extensive mitochondrial swelling with destruction of mitochondrial cristae.

Western blot (WB) assay was further performed to elucidate the mechanism of cell apoptosis induced by PPIX-PEI-UCNP@FA NPs in NIR-triggered PDT [Fig. 4(e)]. Bcl-2 and Bax proteins in the Bcl-2 family played an important regulatory role in cell apoptosis and could mediate the release of cytochrome c (Cyto c) through mitochondria-dependent pathway. The results showed that the increasing intracellular ROS

levels induced by laser irradiation significantly stimulated the up-regulation of apoptosis-associated proteins Bax/Bcl-2 and Cyto c, which were 2.1 times and 3.0 times higher than those in the negative control group, respectively, indicating PPIX-PEI-UCNP@FA NPs in NIR-triggered PDT activated subsequent apoptosis [Fig. 4(f)]. For caspase-3, as one of the most critical apoptotic “executors” downstream of mitochondria-related pathways, its activation was largely dependent on the release of Cyto c. After both NPs and laser irradiation treatment, the relative protein expression of caspase-3 increased. Overall, all these findings demonstrated that PPIX-PEI-UCNP@FA NPs could significantly induce cell apoptosis via caspase-3-mediated mitochondria-dependent pathway in NIR-triggered PDT.

The biosafety of PPIX-PEI-UCNP@FA NPs *in vivo*. The selective killing of tumor cells and significant PDT anticancer properties of PPIX-PEI-UCNP@FA NPs render them promising for *in vivo* tumor therapy. First, the biosafety of PPIX-PEI-UCNP@FA NPs and laser irradiation was evaluated *in vivo*. As illustrated in Fig. 5(a), healthy BALB/c mice were randomly separated into four groups and injected with nanoparticle dispersion or PBS via the tail vein, with the laser group being irradiated the day after injection. The weight of the mice was recorded every two days for 28 days. Throughout the entire treatment period, no notable weight loss was observed after different treatments, but there was an upward trend in body weight, indicating that neither laser irradiation nor PPIX-PEI-UCNP@FA NPs treatment, nor the combination of both, impaired normal mice. In addition, the mice were sacrificed on the 28th day, and the main organs and blood samples of the mice were gathered for follow-up testing. The hematoxylin and eosin (H&E) staining of organs revealed that there was no evident inflammatory cell infiltration and histological damage

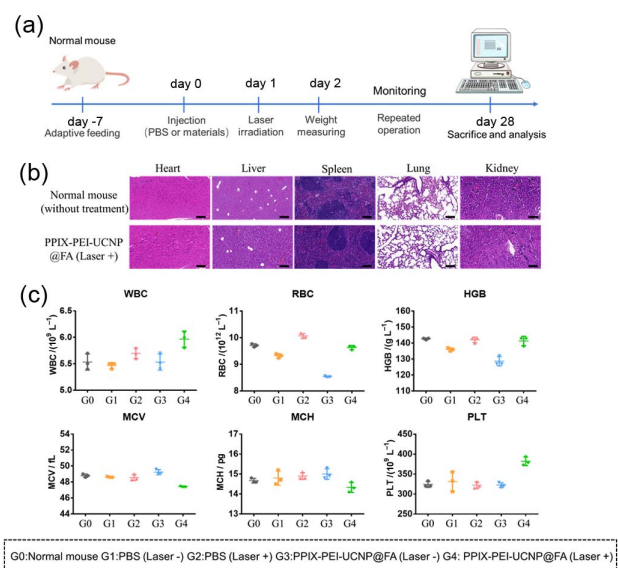


Fig. 5. (a) Treatment protocol for normal BALB/c mice intravenously injected with PBS and PPIX-PEI-UCNP@FA NPs. (b) Representing H&E staining images of major organs (heart, liver, spleen, lung, and kidney) treated with PPIX-PEI-UCNP@FA NPs in the presence of the laser (980 nm, 1 W cm^{-2}) after 28 days (scale bar: 50 μm). (c) Routine blood assay with various treatments at 28 days.

in the major organs (liver, heart, kidney, spleen, and lung) following different treatments as compared to the control group (without any treatment) [Fig. 5(b)]. At the same time, the relevant blood samples were examined for whole blood indexes. It could be seen from the results that the values of red blood cells, white blood cells, and platelets in the whole blood analysis were in a normal range, accompanied with no adverse reaction such as infection, inflammation, and functional injury after different treatments [Fig. 5(c)]. These findings suggested that laser irradiation and PPIX-PEI-UCNP@FA NPs both had favorable biocompatibility and were suitable for *in vivo* investigation.

The anticancer capability of PPIX-PEI-UCNP@FA NPs *in vivo*. In order to verify the PDT anticancer ability of PPIX-PEI-UCNP@FA NPs *in vivo*, 4T1 cells were inoculated subcutaneously in the subcutaneous right forelimb armpit of mice. The establishment of the tumor model and subsequent treatment are illustrated in Fig. 6(a). Initially, PPIX-PEI-UCNP@FA NPs were injected into the tail vein to track the distribution of NPs *in vivo*, as seen in Fig. 6(b) PPIX-PEI-UCNP@FA NPs accumulated at the tumor site. As time

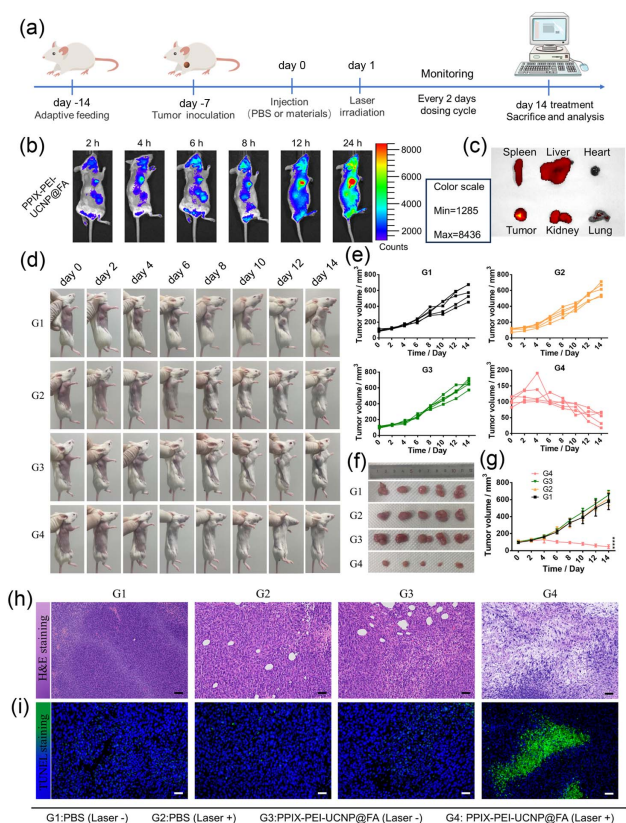


Fig. 6. (a) Schematic diagram of the establishment of a 4T1 tumor model and treatment process. (b) Distribution of PPIX-PEI-UCNP@FA NPs *in vivo* at the scheduled time by an IVIS system. (c) *Ex vivo* imaging of major organs (heart, liver, spleen, lung, and kidney) and tumors at 24 h. (d) Representative photographs of 4T1 tumor mice in different treatment groups on day 0, 2, 4, 6, 8, 10, 12, and 14. (e) Tumor change curve in each treatment group ($n = 5$ for each group). (f) Photographs of tumors after various treatments on day 14. (g) The average tumor volume variation of each group. (h) H&E staining and (i) TUNEL staining images of tumors after different treatments (scale bar: 50 μm).

progressed, the fluorescence emission at the tumor site continuously increased, maximum at 24 h after injection. In addition, *in vitro* fluorescence images of solid tumors at 24 h showed a significantly higher accumulation of NPs compared to major organs [Fig. 6(c)]. These findings showed that PPIX-PEI-UCNP@FA NPs had a good ability to target tumors, and the accumulation ability at the tumor site could help promote PDT.

Then, the 20 subcutaneously injected mice were randomly separated into four groups. In accordance with the *in vitro* experimental groups, G1: PBS (without laser), G1: PBS (with laser), G1: PPIX-PEI-UCNP@FA NPs (without laser), and G1: PPIX-PEI-UCNP@FA NPs (with laser) were selected for the *in vivo* tests. The growth of the tumor in mice over time was monitored by photographing and measuring tumor size [Fig. 6(d)]. It could be seen that the tumor volume of the G1–G3 group showed a trend of progressive growth over time, whereas the tumor volume of the G4 group initially increased little and then continued to decline with the extension of treatment time [Fig. 6(e)]. On the 14th day, the mice were sacrificed, and the tumors were taken out for photographic record [Fig. 6(f)]. By analyzing the change in tumor volume, it is calculated that the tumor inhibition rate of PPIX-PEI-UCNP@FA NPs combined with laser therapy could reach 54.01%. On the other hand, neither the use of NPs nor laser irradiation alone significantly inhibited the growth of tumors [Fig. 6(g)]. Additionally, there was not a noticeable distinction in the weight of the mice among treatment groups. Moreover, the corresponding blood samples on the 14th day of detection also reflected that there were no adverse reactions in the mice after different treatments, and the negative effects of NPs on the metabolism of mice were also negligible.

Histological analysis of tumor tissues and major organs was performed after undergoing various therapies. In all treatment groups, no significant pathological morphological changes were discovered in the major organs (liver, heart, kidney, spleen, and lung), indicating that the treatment group had good biosafety. Representative H&E tumor staining images showed that the cell structure was regularly arranged in the normal saline group (with or without laser) and the PPIX-PEI-UCNP@FA NPs group (without laser), and the nucleus shape was complete and clear. In contrast, in the PPIX-PEI-UCNP@FA NPs plus light treatment group, the tumor tissue was severely damaged, and the nucleus was widely fractured or even disappeared [Fig. 6(h)]. At the same time, TUNEL staining images also demonstrated that the combination treatment group led to the highest levels of apoptosis, as evidenced by the wide dispersion of green regions in Fig. 6(i). In the other three groups, only scattered green fluorescence was present. These results indicated the effective anticancer activity of PPIX-PEI-UCNP@FA NPs *in vivo*, especially when the laser was utilized as a trigger.

3. CONCLUSION

Traditional PDT faces challenges in treating large or deep-seated tumors due to the limited penetration of visible light through thick tissues. To overcome this limitation, near-infrared light has been introduced into the field of PDT,

as its absorption within the biological body is relatively low, thus enabling greater depth of penetration. However, the advancement of two-photon PDT is constrained by the requirement for the simultaneous absorption of two coherent near-infrared photons, leading to lower efficiency and the need for costly pulse lasers. To address this issue, upconversion fluorescence technology has been introduced. It has the capability to convert low-energy near-infrared light into high-energy visible light, matching the activation absorption wavelength of photosensitizers deep in the tissue, while maintaining efficient ROS generation. Compared to conventional two-photon excitation, upconversion fluorescence demonstrates higher efficiency and does not necessitate complex and expensive equipment, making it achievable through cost-effective continuous-wave laser diodes. This approach enables PDT to achieve greater penetration depths while reducing costs, thus becoming a viable option for practical treatment. In this study, we used UCNPs as carriers for PDT drugs, incorporating branched PEI to create a spatial structure centered on UCNP nodes, achieving a PPIX drug loading capacity of 0.69% (mass fraction). This facilitates the efficient generation of ROS in skin tumors (10 mm depth). Both *in vitro* and *in vivo* experiments were conducted, demonstrating that UCNPs can convert 980 nm near-infrared light into visible light, activating the photosensitizer to induce cytotoxic ROS. The results indicate that the PPIX photosensitizer activated by 980 nm light induces tumor cell apoptosis by up-regulating of apoptosis-associated proteins Bax/Bcl-2 as well as mediating the release of cytochrome c and caspase-3 via the mitochondria-related pathway, significantly enhancing the efficacy of PDT and augmenting the tumor-killing effects. Furthermore, the combination of FA and PPIX-PEI-UCNP complexes for targeted tumor treatment further enhances PDT's specific cytotoxicity. The exceptional performance underscores the potential of PPIX-PEI-UCNP@FA NPs to play a role in clinical treatment of deep-seated tumors.

APPENDIX A: MATERIALS AND METHODS

Synthesis of PPIX-PEI-UCNP@FA NPs.

1) Preparation of NaYF₄:18%Yb,2%Er

A total of 1 mmol of rare earth chlorides (0.80 mmol yttrium chloride, 0.18 mmol erbium chloride, 0.02 mmol erbium chloride) was placed in a three-neck flask with a capacity of 100 mL. Subsequently, 6 mL of oleic acid and 15 mL of octadecene were added. The mixture was heated under an argon atmosphere to 160°C and allowed to react for 60 min. Then, it was cooled to room temperature. A solution containing 4 mmol of ammonium fluoride and 2.5 mmol of sodium hydroxide in 10 mL of methanol was prepared and added dropwise to the reaction system. The mixture was stirred at room temperature for 60 min before raising the temperature to 60°C and maintaining the reaction for another 60 min. Following that, the temperature of the system was rapidly increased to 300°C and kept at that temperature for 60 min under an argon atmosphere. Finally, the temperature of the system was allowed to cool naturally to room temperature. Excess anhydrous ethanol was added to the reaction system to precipitate the

product, which was then centrifuged three times at a speed of 8000 r/min. The resulting product was dispersed in *n*-hexane for subsequent use.

2) Preparation of NaYF₄:18%Yb,2%Er@NaYF₄

A total of 0.5 mmol of yttrium chloride solid was combined with 6 mL of oleic acid and 15 mL of octadecene. The mixture was heated under an argon atmosphere to 160°C and allowed to react for 60 min. It was then cooled to room temperature. The previously prepared NaYF₄:18%Yb,2%Er nanomaterial was dispersed in 8 mL of *n*-hexane and added to the reaction system. The mixture was stirred at this temperature for 30 min. Subsequently, a solution containing 2 mmol of ammonium fluoride and 1.25 mmol of sodium hydroxide in 10 mL of methanol was added dropwise to the reaction system. The mixture was stirred at room temperature for 60 min before raising the temperature to 60°C and maintaining the reaction for 30 min. After that, the temperature of the system was rapidly increased to 300°C and kept at that temperature for 60 min under an argon atmosphere. Finally, the temperature of the system was allowed to cool naturally to room temperature. Excess anhydrous ethanol was added to the reaction system to precipitate the product, which was then centrifuged three times at a speed of 8000 r/min. The resulting product was dispersed in *n*-hexane for subsequent use.

3) Preparation of NaYF₄:18%Yb,2%Er@NaYF₄ (UCNP)-PPIX

Synthesized NaYF₄:18%Yb,2%Er@NaYF₄ nanoparticles were collected by centrifugation and dispersed in 50 mL of anhydrous methanol with 500 mg of the particles. Surface functionalization was conducted by adding 10 mmol APTES and 55 mmol MPTMS, followed by stirring under an argon atmosphere at room temperature for 24 h to ensure complete silanization. Unreacted silane agents were removed by centrifugation (10,000 r/min, 10 min). The UCNPs were redispersed in 50 mL of anhydrous methanol, followed by the addition of 10 mL of 30% hydrogen peroxide and stirring for another 12 h at room temperature to oxidize thiol groups to carboxyl groups. Afterward, centrifugation and washing with ultrapure water were performed at least three times to remove any remaining hydrogen peroxide.

To prepare the PPIX solution, 0.1 g of PPIX was dissolved in 100 mL of DCM to create a 1 mg/mL solution. A PBS solution containing double the molar amount of EDC and NHS was prepared. EDC/NHS solution was added slowly to the PPIX solution and stirred at room temperature for 1 h. This solution was then added to the above-modified UCNPs and mixed by stirring at room temperature for 24 h. Unreacted PPIX and solvent were removed by centrifugation (8500 r/min, 15 min). The UCNPs were then washed with ultrapure water, repeated more than three times.

4) Preparation of NaYF₄:18%Yb,2%Er@NaYF₄ (UCNP)-PPIX-PEI

0.1 g of PEI was dissolved in 100 mL of ultrapure water to prepare a 1 mg/mL PEI solution, to which 1.5 mg of EDC and 0.1 mg of NHS were added. The mixture was stirred at room

temperature for 30 min before being added to the UCNP suspension modified with PPIX. Electron beam irradiation of the solution was performed (3 MeV voltage, total dose of 100 kGy, dose rate of 2 kGy/min) for 50 min. The reaction was further stirred for 4 h at room temperature to form the PEI-linked UCNP complex. An additional 0.05 mL of activated PPIX was introduced to the reaction, adjusting the pH to neutral to maximize the reactivity of amine groups and prevent carboxyl protonation. The mixture was stirred overnight at room temperature. Centrifugation (10,000 r/min, 10 min) was used to remove unreacted PEI and PPIX. The complex was washed with ultrapure water, repeated more than three times. The washed complex was then transferred to a dialysis bag and dialyzed against PBS or ultrapure water for 48 h to remove small molecular impurities. The dialyzed complex was dried in a vacuum oven at 40°C for 12 h.

5) Preparation of NaYF₄:18%Yb,2%Er@NaYF₄ (UCNP)-PPIX-PEI-FA

20 mg of folic acid was ultrasonically dispersed in 10 mL of MES buffer. To this mixture, 80 mg of EDC and 120 mg of NHS were added, followed by ultrasonication for 15 s. The mixture was then sealed with a film and incubated on a shaker at 37°C for 15 min. The composite particles prepared in step (4) were introduced into the reaction system, ultrasonicated rapidly for 1 min, and then transferred to a shaker at 37°C for 12 h. An additional 0.05 mL of activated PPIX was subsequently added to the mixture, which then reacted on the shaker for another 4 h. Upon completion of the reaction, the product was washed with deionized water and centrifuged (8000 r/min), repeated three times to obtain the final product (PPIX-PEI-UCNP@FA).

Characterization of PPIX-PEI-UCNP@FA NPs.

1) Transmission electron microscopy (TEM) measurement

A suitable quantity of PPIX-PEI-UCNP@FA NPs were subjected to ultrasonic cleaning for a duration of at least 5 min in an ultrasonic cleaner. Subsequently, 5 μL of the solution was deposited onto a thin carbon film supported on a copper grid. After drying, the morphology of the samples was observed using the Thermo Fisher TALOS F200X 200 kV transmission electron microscope, followed by energy dispersive X-ray spectroscopy (EDS) elemental analysis and mapping surface scan measurements.

2) Fourier-transform infrared spectroscopy (FTIR) analysis

A predetermined quantity of dried PPIX-PEI-UCNP@FA NPs were ground and pressed into pellets. The structural characterization of the magnetic nanoparticles was conducted using the Thermo Fisher Nicolet 6700 Fourier-transform infrared spectrometer over a scanning range of 700 cm⁻¹ to 4000 cm⁻¹.

3) Ultraviolet-visible absorption spectroscopy measurement

The ultraviolet-visible absorption spectra of the samples were recorded using the Thermo Fisher EV300 UV-Vis spectrophotometer.

4) Fluorescence spectroscopy (PL) measurement

Sample testing was carried out using the FLS1000 steady-state and transient fluorescence spectrometer from Edinburgh Instruments, United Kingdom.

5) Zeta potential and particle size measurement

The particle size, distribution, and surface potential of the samples were determined using the NanoBrook Omni Nanosizer for zeta potential measurements.

Cell cultures. Normal mouse fibroblast (L929) cells and mouse breast cancer (4T1) cells were brought from ATCC. L929 cells and 4T1 cells were cultured in the RPMI-1640 medium and DMEM/high glucose medium, respectively, containing 10% FBS and 1% penicillin-streptomycin (Gibco). All cells were incubated in the incubator at 37°C supplemented with 5% CO₂.

In vitro cell viability and PDT effect. To evaluate the cytotoxicity of PPIX-PEI-UCNP@FA NPs to cells, a CCK-8 (Cell Counting Kit 8) assay was first performed. Briefly, L929 and 4T1 cells were seeded into 96-well plates at a density of 2×10^4 cells/well and then incubated with various concentration PPIX-PEI-UCNP@FA NPs for various times (24 h, 48 h, and 72 h). Notably, in order to eliminate interference during laser irradiation, cells with and without laser irradiation were seeded on different 96-well plates. The L929 and 4T1 cells were irradiated for 10 min every day. Afterwards, the CCK-8 test was carried out in accordance with the standard instructions and the optical density value (450 nm) was assessed using a microplate reader (TECAN Infinite 200 PRO). The relative cell viability (%) was calculated according to Eq. (1),

$$\text{Cell viability(\%)} = [(A_s - A_b)/(A_c - A_b)] \times 100\%, \quad (1)$$

where A_s is the absorbance of the experimental well containing cell culture medium CCK-8 and the substance to be tested. A_b is the absorbance of a blank well, without the cell culture medium, CCK-8, and substance. A_c is the absorbance of the control group, containing the cell culture medium and CCK-8 without the substance to be tested.

Then, a live/dead test was performed. The L929 and 4T1 cells were seeded onto 24-well plates (1×10^5 cells per well) and cultured with PPIX-PEI-UCNP@FA NPs (60 µg/mL) for 48 h. Every day for 10 min, the L929 and 4T1 cells were exposed to radiation. Afterwards, the cells were stained with calcein-AM and PI (2 and 4 µmol/L) for 30 min. A fluorescent microscope (Olympus IX73) was employed to view fluorescence images of live/dead staining.

Flow cytometry for cell apoptosis evaluation. The 4T1 cells were seeded onto 6-well plates (5×10^5 cells per well) and divided into four groups as follows: cells without laser and PPIX-PEI-UCNP@FA NPs; cells with laser but without PPIX-PEI-UCNP@FA NPs; cells without laser but incubated with PPIX-PEI-UCNP@FA NPs (60 µg/mL) for 24 h; and cells with laser and incubated with PPIX-PEI-UCNP@FA NPs (60 µg/mL) for 24 h. For cell apoptosis analysis, the cells were labeled with FITC-annexin V and propidium iodide (PI) in line with the manufacturer's instructions and measured by a flow cytometer (CytoFLEX LX, Beckman Coulter). All data were analyzed using a FlowJo software (Treestar, USA).

The detection of intracellular ROS generation. To assess the generation of ROS, 2',7'-dichlorofluorescein diacetate (DCFH-DA) as an ROS probe was used. The 4T1 cells were seeded onto 6-well plates (5×10^5 cells per well) and incubated with PPIX-PEI-UCNP@FA NPs (60 µg/mL) in the dark. The 4T1 cells treated with H₂O₂ (100 µmol/L) were regarded as the positive control. Then, the 4T1 cells were rinsed with PBS to remove uninternalized NPs, and fresh culture media with DCFH-DA (20 µmol/L) was added for an additional 45 min of incubation in the incubator without light. The 4T1 cells were exposed to NIR laser light (980 nm, 1.0 W cm⁻²) for 10 min and collected by trypsinization for the subsequent flow cytometry test. FlowJo software was used to examine all of the data. For 4T1 cells that did not require digestion, imaging was directly performed using a fluorescence microscope.

In vitro TUNEL staining experiment. The 4T1 cells were initially inoculated onto 96-well plates (2×10^4 cells per well) and then cultured with PPIX-PEI-UCNP@FA NPs (60 µg/mL). After different treatments, cells were washed with PBS and stained with TUNEL kit according to the standard protocol. The imaging was performed under a fluorescence microscope.

Cell uptake and localization of PPIX-PEI-UCNP@FA NPs. The cell uptake and co-localization of PPIX-PEI-UCNP@FA NPs were performed using a laser scanning confocal microscope (Leica SP8 STED, German), a flow cytometer, and a fluorescence microscope, respectively. The 4T1 cells were seeded in 20 mm plates at a density of 5×10^4 cells per well and then incubated with PPIX-PEI-UCNP@FA NPs (60 µg/mL) for various times. Afterwards, the cells were washed with fresh PBS and labeled with Hoechst 33342 for further fluorescence observation.

For flow cytometry detection, the 4T1 cells were seeded onto 6-well plates (5×10^5 cells per well) followed by incubating with PPIX-PEI-UCNP@FA NPs (60 µg/mL) for various times. Then, cells were rinsed with fresh PBS to eliminate uninternalized NPs and trypsinized to collect cells. Cell suspensions were prepared by washing the cells with PBS several times and adding new PBS for flow cytometry.

The ability of PPIX-PEI-UCNP@FA NPs targeting to mitochondria. The 4T1 cells were seeded in 20 mm confocal dishes (5×10^4 cells per well) and then incubated with PPIX-PEI-UCNP@FA NPs. After being washed with warmed PBS several times, 4T1 cells were labeled with MitoTracker Green (100 nmol/L) and incubated at 37°C for 30 min in the incubator. Following multiple PBS washes, the cells were observed by CLSM.

Detection of mitochondrial ROS generation. After different treatments, according to the standard procedure, the MitoSOX™ red (100 nmol/L) mitochondrial indicator was employed to monitor the production of superoxides in mitochondria, together with MitoTracker Green staining mitochondria to detect the production of ROS in mitochondria. All the fluorescence images were captured by CLSM.

Mitochondrial injury evaluation. The effect of PDT on mitochondria was evaluated by changes in mitochondrial membrane potential and mitochondrial morphology. The 4T1 cells (5×10^5 cells) were seeded onto 6-well plates and separated

into different groups. After different treatments, the cells were washed with PBS three times, stained with the JC-1 probe for 30 min, and finally characterized with a fluorescence microscope. For quantitative analysis, the digested cell suspension was loaded with the JC-1 probe and detected by flow cytometry.

The 4T1 cells (5×10^5 cells) were seeded onto 6-well plates and cultured with PPIX-PEI-UCNP@FA NPs overnight. After being fixed in PBS containing 2.5% glutaraldehyde according to the standard protocol, the mitochondrial morphology of cells was observed using the biological transmission electron microscopy (TEM, Tecnai G2).

Western blot analysis. After various treatments, total proteins of 4T1 cells were obtained using the RIPA lysis buffer (Bryotime, China) and then measured with a BCA kit (Bryotime, China) in accordance with the manufacturer's instructions. In the following step, the protein samples were separated using SDS-PAGE (sodium dodecyl sulfate-polyacrylamide gel electrophoresis) and moved onto poly(vinylidene fluoride) (PVDF) membranes (Millipore, USA). The membranes were treated overnight at 4°C with specific primary antibodies, including Bax (1:2000), Bcl-2 (1:1000), cytochrome (1:2000), caspase-3 (1:1000), and β -actin (1:5000), following blocking with non-fat dry milk (5%) for 2 h. These PVDF membranes were then treated for an hour at room temperature with the matching secondary antibodies (1:2000). After another TBST (Tris buffered saline with Tween-20) washing, the membranes were examined using gel imaging equipment (Fusion FX7, France).

Animals. BALB/c mice (female, 3–5 weeks) were obtained from Shanghai Lingchang Biotechnology Co., Ltd. (Shanghai, China). All animal studies were carried out in accordance with procedures that had been approved by Shanghai Jiao Tong University's Ethical Committee for Animal Experiments (China, A2023044).

In vivo biosafety of PPIX-PEI-UCNP@FA NPs. In order to evaluate the biocompatibility of PPIX-PEI-UCNP@FA NPs *in vivo*, healthy female BALB/c mice were randomly divided into five groups as follows: G0, normal group; G1, PBS (without laser); G2, PBS (with laser); G3, PPIX-PEI-UCNP@FA NPs (without laser); and G4, PPIX-PEI-UCNP@FA NPs (with laser). All the solutions were injected via the tail vein every 2 days for 4 weeks. The mice were weighed every two days and sacrificed 28 days after the injection. To assess the potential toxicity of NPs, major organs with post-treatment, such as the heart, liver, spleen, kidney, and lung, were collected. All samples were fixed with a 4% paraformaldehyde solution, sliced, and then stained with hematoxylin and eosin (H&E) for histological analysis. Corresponding blood samples were also collected for whole blood analysis tests.

Establishment of subcutaneous tumor model. To establish subcutaneous tumor model, 4T1 cell suspension (1×10^6 cells) was initially inoculated subcutaneously in the subcutaneous right forelimb armpit of female BALB/c mice. After 7 days of feeding, the mice were randomly divided into four groups ($n = 5$ per group) for follow-up experiments as follows: G1, PBS (without laser); G2, PBS (with laser); G3, PPIX-PEI-UCNP@FA NPs (without laser); and G4, PPIX-PEI-UCNP@FA NPs (with laser).

Anticancer effect of PPIX-PEI-UCNP@FA NPs *in vivo*.

The PDT effect of NPs was evaluated in the subcutaneous tumor model. Both the sterile PBS solution and the NP suspension were injected through the tail vein every 2 days for 4 weeks. The group that needed light therapy was exposed to the NIR laser for 10 min. Meanwhile, the weight of the mice in all groups was recorded every 2 days, and the tumor changes in the mice were photographed by camera.

In vivo imaging and biodistribution of PPIX-PEI-UCNP@FA NPs. Female BALB/c mice with subcutaneous tumor models were administered intravenous injections of PPIX-PEI-UCNP@FA NPs. The fluorescence imaging of mice using the IVIS system from PerkinElmer (Ex: 710 nm; Em: 800 nm) was used to determine the distribution of PPIX-PEI-UCNP@FA NPs at various time intervals (2, 4, 6, 8, 12, and 24 h). After 24 h, the mice were sacrificed, and the major organs (lungs, kidneys, hearts, spleens, and livers) and tumor tissues were excised and imaged *ex vivo* (Ex: 710 nm; Em: 800 nm).

Histological and TUNEL staining analysis. For histological analysis, all mice were sacrificed on day 14. The tumor tissues were stripped, and major organs were collected. The specimens were fixed with PFA (4%), and histological sections were prepared. Additionally, these sections were visualized by H&E staining.

For TUNEL staining analysis, the slides were stained with TUNEL in accordance with the approved method. The stained slides were imaged using a fluorescence microscope (80i, Nikon).

Statistical analysis. The mean values together with the standard deviation (SD) were used to display all experimental results. Statistical analysis was utilized to analyze the differences between groups with a *t*-test (2-tailed) using the GraphPad Software (Version 6). The statistical significance was provided as * $p < 0.05$, ** $p < 0.01$, *** $p < 0.001$, and **** $p < 0.0001$, respectively.

Funding. Natural Science Foundation of Shanghai Municipality (23ZR1428400); Shanghai Municipal Science and Technology Major Project (2019SHZDZX01-06); National Natural Science Foundation of China (12104298, 12192252).

Acknowledgment. The authors acknowledge support from the state Key Laboratory on Fiber Optic Local Area Communication Networks and State Key Laboratory of Metal Matrix Composites, and they also thank the Ruijin Hospital.

Disclosures. The authors declare no conflicts of interest.

Data Availability. Data underlying the results presented in this paper are not publicly available at this time but may be obtained from the authors upon reasonable request.

REFERENCES

1. R. R. Allison and C. H. Sibata, "Oncologic photodynamic therapy photosensitizers: a clinical review," *Photodiagn. Photodyn. Ther.* **7**, 61–75 (2010).
2. S. Kwiatkowski, B. Knap, D. Przystupski, *et al.*, "Photodynamic therapy: mechanisms, photosensitizers and combinations," *Biomed. Pharmacother. Biomed. Pharmacother.* **106**, 1098–1107 (2018).

3. C. Sisi, Y. Deyan, C. Yuqi, *et al.*, "In vivo targeted deep-tissue photodynamic therapy based on near-infrared light triggered upconversion nanoconstruct," *ACS Nano* **71**, 676–688 (2013).
4. M. Mitsunaga, M. Ogawa, N. Kosaka, *et al.*, "Cancer cell-selective in vivo near infrared photoimmunotherapy targeting specific membrane molecules," *Nat. Med.* **17**, 1685–1691 (2011).
5. G. Liu, J. Sheng, and Y. Zhao, "In vivo near-infrared fluorescence imaging," in *Nanotechnology Characterization Tools for Biosensing and Medical Diagnosis* (Springer, 2018), pp. 537–577.
6. Z. Peng, W. Steelant, K. Manoj, *et al.*, "Versatile photosensitizers for photodynamic therapy at infrared excitation," *J. Am. Chem. Soc.* **129**, 4526–4527 (2007).
7. C. S. Qi, D. Yuchen, D. M. Sagar, *et al.*, "Photon upconversion towards applications in energy conversion and bioimaging," *Prog. Surf. Sci.* **92**, 281–316 (2017).
8. J. Xu, W. Han, P. Yang, *et al.*, "Tumor microenvironment-responsive mesoporous MnO₂-coated upconversion nanoplatform for self-enhanced tumor theranostics," *Adv. Funct. Mater.* **28**, 1803804 (2018).
9. W. Chao, T. Huiquan, C. Liang, *et al.*, "Near-infrared light induced in vivo photodynamic therapy of cancer based on upconversion nanoparticles," *Biomaterials* **32**, 6145–6154 (2011).
10. D. K. Chatterjee and Z. Yong, "Upconverting nanoparticles as nanotransducers for photodynamic therapy in cancer cells," *Nanomedicine* **3**, 73–82 (2008).
11. F. Wang, D. Banerjee, Y. Liu, *et al.*, "Upconversion nanoparticles in biological labeling, imaging, and therapy," *Analyst* **135**, 1839–1854 (2010).
12. C. Wang, L. Cheng, and Z. Liu, "Upconversion nanoparticles for potential cancer theranostics," *Ther. Deliv.* **2**, 1235–1239 (2011).
13. H. Qian, G. Hui, P. Ho, *et al.*, "Mesoporous-silica-coated up-conversion fluorescent nanoparticles for photodynamic therapy," *Small* **5**, 2285–2290 (2009).
14. N. M. Idris, M. K. Gnanasammandhan, Z. Jing, *et al.*, "In vivo photodynamic therapy using upconversion nanoparticles as remote-controlled nanotransducers," *Nat. Med.* **18**, 1580–1585 (2012).
15. X. Lu, X. Kong, L. Xiaomin, *et al.*, "An upconversion nanoparticle–zinc phthalocyanine based nanophotosensitizer for photodynamic therapy," *Biomaterials* **35**, 4146–4156 (2014).
16. L. Yanyan, M. Xianfu, and W. Bu, "Upconversion-based photodynamic cancer therapy," *Coord. Chem. Rev.* **379**, 82–98 (2017).
17. M. Lin, Y. Zhao, S. Q. Wang, *et al.*, "Recent advances in synthesis and surface modification of lanthanide-doped upconversion nanoparticles for biomedical applications," *Biotechnol. Adv.* **30**, 1551–1561 (2012).
18. G. Chen, H. Qiu, P. N. Prasad, *et al.*, "Upconversion nanoparticles: design, nanochemistry, and applications in theranostics," *Chem. Rev.* **114**, 5161–5214 (2014).
19. X. Chen, D. Peng, Q. Ju, *et al.*, "Photon upconversion in core–shell nanoparticles," *Chem. Soc. Rev.* **44**, 1318–1330 (2015).
20. F. Auzel, "Upconversion and anti-Stokes processes with f and d ions in solids," *Chem. Rev.* **104**, 139–173 (2004).
21. Z. Jing, L. Qian, F. Wei, *et al.*, "Upconversion luminescent materials: advances and applications," *Chem. Rev.* **115**, 2350–2465 (2015).
22. X. Wu, Y. Zhang, K. Takle, *et al.*, "Dye-sensitized core/active shell upconversion nanoparticles for optogenetics and bioimaging applications," *ACS Nano* **10**, 1060 (2016).
23. D. Chatterjee, A. J. Rufaihah, and Y. Zhang, "Upconversion fluorescence imaging of cells and small animals using lanthanide doped nanocrystals," *Biomaterials* **29**, 937–943 (2008).
24. Z. Chen, H. Chen, H. Hu, *et al.*, "Versatile synthesis strategy for carboxylic acid-functionalized upconverting nanophosphors as biological labels," *J. Am. Chem. Soc.* **130**, 3023–3029 (2008).
25. K. Liu, X. Liu, Q. Zeng, *et al.*, "Covalently assembled NIR nanoplatform for simultaneous fluorescence imaging and photodynamic therapy of cancer cells," *ACS Nano* **6**, 4054–4062 (2012).
26. C. Wang, L. Cheng, and Z. Liu, "Upconversion nanoparticles for photodynamic therapy and other cancer therapeutics," *Theranostics* **3**, 317–330 (2013).
27. M. Wang, C. C. Mi, W. X. Wang, *et al.*, "Immunolabeling and NIR-excited fluorescent imaging of HeLa cells by using NaYF₄:Yb,Er up-conversion nanoparticles," *ACS Nano* **3**, 1580–1586 (2009).
28. L. Xiong, Z. Chen, Q. Tian, *et al.*, "High contrast upconversion luminescence targeted imaging in vivo using peptide-labeled nanophosphors," *Anal. Chem.* **81**, 8687–8694 (2009).
29. C. Wang, L. Cheng, Y. Liu, *et al.*, "Imaging-guided pH-sensitive photodynamic therapy using charge reversible upconversion nanoparticles under near-infrared light," *Adv. Funct. Mater.* **23**, 3077–3086 (2013).
30. F. Wenpei, W. Bu, and S. Jianlin, "On the latest three-stage development of nanomedicines based on upconversion nanoparticles," *Adv. Mater.* **28**, 3977 (2016).
31. C. Song, S. Zhang, and Q. Zhou, "Upconversion nanoparticles for bio-imaging," *Nanotechnol. Rev.* **6**, 233–242 (2017).
32. X. Jia, J. Yin, D. He, *et al.*, "Polyacrylic acid modified upconversion nanoparticles for simultaneous pH-triggered drug delivery and release imaging," *J. Biomed. Nanotechnol.* **9**, 2063–2072 (2013).
33. L. Cheng, C. Wang, and Z. Liu, "Upconversion nanoparticles and their composite nanostructures for biomedical imaging and cancer therapy," *Nanoscale* **5**, 23–37 (2012).
34. G. Arif, J. Xu, P. Yang, *et al.*, "Upconversion processes: versatile biological applications and biosafety," *Nanoscale* **9**, 12248–12282 (2017).
35. X. Zhang, W. Xie, X. Li, *et al.*, "Boosting luminance energy transfer efficiency in upconversion nanoparticles with an energy-concentrating zone," *Angew. Chem.* **58**, 12117–12122 (2019).
36. J. C. Kennedy and R. H. Pottier, "Endogenous protoporphyrin IX, a clinically useful photosensitizer for photodynamic therapy," *J. Photochem Photobiol. B* **14**, 275–292 (1992).
37. D. E. J. G. J. Dolmans, D. Fukumura, and R. K. Jain, "Photodynamic therapy for cancer," *Nat. Rev. Cancer* **3**, 380–387 (2003).
38. E. S. Nyman and P. H. Hynninen, "Research advances in the use of tetrapyrrolic photosensitizers for photodynamic therapy," *J. Photochem. Photobiol. B* **73**, 1–28 (2004).
39. A. F. McDonagh and L. A. Palma, "Tin-protoporphyrin: a potent photosensitizer of bilirubin destruction," *Photochem. Photobiol.* **42**, 261–264 (2010).
40. J. Kou, D. Dou, and L. Yang, "Porphyrin photosensitizers in photodynamic therapy and its applications," *Oncotarget* **8**, 81591–81603 (2017).
41. C. Sun, L. Bao, Y. Zhao, *et al.*, "A photosensitizer discretely loaded nanoaggregate with robust photodynamic effect for local treatment triggers systemic antitumor responses," *ACS Nano* **16**, 3070–3080 (2022).
42. G. L. Zwicke, G. A. M. Fau, C. J. Jeffery, *et al.*, "Utilizing the folate receptor for active targeting of cancer nanotherapeutics," *Nano Rev.* **3**, 18496 (2012).
43. E. Anna, A. N. Guller, A. N. Generalova, *et al.*, "Rational surface design of upconversion nanoparticles with polyethylenimine coating for biomedical applications: better safe than brighter?" *ACS Biomater. Sci. Eng.* **4**, 3143–3153 (2018).
44. M. Prieto, A. Y. Rwei, T. Alejo, *et al.*, "Light emitting photon upconversion nanoparticles in the generation of transdermal reactive oxygen species," *ACS Appl. Mater. Interfaces* **9**, 41737–41747 (2017).